



Numerical modeling techniques for noise emission of free railway wheels

Linus Taenzer¹ · Urs Pachale¹ · Bart Van Damme¹ · Andrea Bergamini¹ · Domenico Tallarico¹

Received: 23 January 2023 / Revised: 30 November 2023 / Accepted: 6 December 2023
© The Author(s) 2024

Abstract

In this article, we consider the numerical prediction of the noise emission from a wheelset in laboratory conditions. We focus on the fluid–structure interaction leading to sound emission in the fluid domain by analyzing three different methods to account for acoustic sources. These are a discretized baffled piston using the discrete calculation method (DCM), a closed cylindrical volume using the boundary element method (BEM) and radiating elastic disks in a cubic enclosure solved with the finite element method (FEM). We provide the validation of the baffled piston and the BEM using measurements of the noise emission of a railway wheel by considering ground reflections in the numerical models. Selected space-resolved waveforms are compared with experimental results as well as with a fluid–structure interaction finite element model. The computational advantage of a discretized disk mounted on a baffle and BEM compared to FEM is highlighted, and the baffled pistons limitations caused by a lack of edge radiation effects are investigated.

Keywords Discretized baffled piston · Finite element · Boundary element · Railway noise · Acoustic emission · Vibrations

1 Introduction

Present research in railway noise tackles various areas such as noise emission caused by aerodynamics, structure-borne sound, electric machines, ground vibration and rolling noise. Particularly, rolling noise has been a widely spread research topic for many years since it is dominant for trains driving at average speeds. In normal rolling conditions, the combined roughness of wheel and rail is the key mechanism of sound generation [1]. Particular challenges can arise with worn wheels, where so-called wheel flats or polygonization lead to particularly high noise generation [2, 3]. Many groups have been investigating the vibrations and sound radiation of train wheels. Particularly, the influence of the rolling contact and additional track effects such as sleeper behavior and ballast reflections have been considered [4–6].

Since the reduction of railway noise requires the consideration of many different physical phenomena and technological aspects, a wide variety of noise abatement measures are possible. Rolling noise dominates the sound emission

between 30 and 250 km/h [7]. Therefore, the wheel–rail interaction is often considered in terms of its subcomponents to study their contribution in more detail and can be optimized by redesigning the parts that strongly contribute to the noise such as the wheel [8–10]. To deal with public requirements and regulations, there is an increasing demand for physics-based models since they are cheap and fast compared to large measurement campaigns.

For the investigation of railway noise, analytical, numerical and experimental methods are available. Sound emission from train wheelsets has been modeled via several analytical [11] and numerical (finite element method (FEM) and boundary element method (BEM)) [2, 12, 13]) techniques. To calculate the vibrational response of train wheels, simplified analytical models exist, assuming a rigid mass and a point sound source for predicting the estimated sound radiation [11]. Adding more complex geometries but still keeping the computational effort low, axial symmetry is exploited, e.g., the waveguide finite element formulation for axisymmetric bodies [14]. Nevertheless, when considering point excitation at the wheel–rail contact interface, the exploitation of axisymmetry alone is insufficient for conducting harmonic analysis. It needs incorporation of approaches such as 2.5D methods [12, 15]. In [12], the vibrational response of the wheel is obtained by using a 2.5D FEM

✉ Linus Taenzer
linus.taenzer@empa.ch

¹ Laboratory of Acoustics/ Noise Control, Empa,
Überlandstrasse 129, Dübendorf, Switzerland

model, and its output is used for a boundary element model. The authors show measurements of a plate to validate their method and then apply it to a railway wheel and show radiation efficiency and peak frequencies. In the work of Fabre et al. [15], a waveguide FEM combined with the Fourier BEM is used to examine the impact of reflective planes on the sound radiation of railway wheels. The authors state that the radiation characteristics stay mostly unchanged when the reflective plane is included. Valid results in the range of 150–10,000 Hz are obtained. For validation, they use a suspended disk in a fully anechoic room with a shaker as an excitation source.

In general, both the axisymmetric and 3D finite element methods are appropriate models to perform computationally feasible vibration calculations for geometries such as railway wheels. However, in the acoustic domain, the computational effort for receiver points at large distances (a common standard is 7.5 m away from the centerline of the railway track [16]) makes finite element simulations very challenging due to the domain size and therefore the BEM is preferable. With the BEM, complex geometries can be investigated, but precise meshes for closed surfaces are needed. Reference [17] presents a notable study that employs BEM, where the author compares distinct sound radiation attributes of wheel modes occurring during curve squealing, focusing on the evaluation of radiation efficiency and directivity. To investigate different wheel profiles, the author of [18] uses the axisymmetry of the wheel for an axiharmonic formulation. Open-source BEM implementations are readily available and allow to avoid time-intensive development of in-house codes [19].

In the field of building acoustics, it is customary to model the radiation of sound assuming a piston mounted on a baffle. This is generally used in cases where the velocity over the piston surface is constant. However, several authors developed expressions for a discretized vibrating piston with non-uniform velocity using analytical solutions [20] or asymptotic expressions for calculating the mutual impedance between the rectangular [21] or circular [22] discretized elements of the oscillating plate. In the study of railway wheels, the baffled piston has been explored in [10] and [23]. Railway wheels are discretized into smaller baffles and the pressure at specific distances can be obtained through integration over each individual subbaffle. This is done using a discretized Rayleigh integral (DRI). Thompson [10] uses the acceleration spectra from five points on two distinct railway wheels to approximate the levels across five concentric rings. In [23], the radiation efficiency and directionality of different wheel types are calculated using a discretized piston segmented into small subbaffles. Despite this, both investigations only account for the self-radiation impedance, as described by the Rayleigh integral, and disregard the mutual radiation impedance as defined by

Stepanishen [22]. A precise and holistic formulation of the impedance of a discretized baffled piston, also known as discrete calculation method (DCM), is presented in [24]. To the best of our knowledge, DCM is used for evaluating the overall radiation efficiency from experimental data [25] and not for radiation patterns. There is no work available comparing DCM for the acoustic impedance connecting acoustic pressure and structural velocity.

The goal of this work is to show that the DCM and the associated impedance matrix can be used to reduce the computational effort and simplify the entire model significantly. To better understand the assumptions of the DCM method used for the baffled piston, we review in Sect. 2 its derivation and compare it to the more standard BEM and FE method in the acoustic domain. We put special emphasis on calculating the impedance matrix that relates sound pressure and normal velocities of the vibrating wheelset, which is common in all three methods. In Sects. 3 and 4 a detailed validation of the vibrometric and acoustic models is presented. This provides the possibility to show a comprehensive comparison between the methods and explains the strengths and limitations of the baffled piston assumptions.

2 Numerical methods for sound radiation

In our approach, the modeling of sound radiation of a wheelset follows two steps: the structural response to an input force calculated using FEM and the propagation in the acoustic domain according to three different methods. The structural finite element model is introduced in order to calculate the velocities of the acoustic source. Three different models representing the acoustic domain (DCM, BEM and FEM) are presented in order to calculate the emitting sound pressure from the previously obtained structural velocities. This procedure is valid since the railway wheel is a heavy structure in the acoustic domain considering air as light fluid. No back-coupling from fluid to structural domain is required since pressure changes on the fluid side are negligibly small. Thus, the system can be solved in two consecutive steps.

2.1 Harmonic finite element analysis for vibrational input data

The theory for time-harmonic analysis in finite elements is based on the equation of motion:

$$\hat{M}\ddot{u}(t) + \hat{C}\dot{u}(t) + \hat{K}u(t) = f(t), \quad (1)$$

solving for displacement u with mass matrix \hat{M} , damping matrix \hat{C} , stiffness matrix \hat{K} and the external force f . Using

$\bar{\mathbf{u}}(t) = \mathbf{u}e^{-j\omega t}$ and $\bar{\mathbf{f}}(t) = \mathbf{f}e^{-j\omega t}$ with amplitudes \mathbf{u} and \mathbf{f} in Eq. (1) yields

$$(-\omega^2 \hat{\mathbf{M}} - j\omega \hat{\mathbf{C}} + \hat{\mathbf{K}})\mathbf{u} = \mathbf{f}, \quad (2)$$

where ω is the angular frequency and j is the imaginary unit. The traditional convention of the equation of motion is commonly obtained using the time-dependent factor $e^{j\omega t}$ instead of $e^{-j\omega t}$. In order to be consistent with wave-propagation studies in the acoustic domain, the notation $e^{-j\omega t}$ is used. The wheel is excited at one specific node at the wheel rim with unit force \mathbf{f} and the displacements \mathbf{u} are calculated using the finite element method in Ansys. From the harmonic analysis, the velocity field \mathbf{v}_s on the surface can be obtained with

$$\mathbf{v}_s = -j\omega \mathbf{u}_s, \quad (3)$$

by extracting the displacement field \mathbf{u}_s on the surface.

In the time-harmonic structural analysis, the steel wheel (see Fig. 1) is excited by a time-harmonic force in order to calculate its frequency response and associated waveforms, shown in panel (Fig. 1a). The excitation takes place at the rim (see blue arrow in Fig. 1a) for axial forces or at one point at the tread (red arrow) for radial forces in order to act consistently with the experiments that follow at a later step. In the second step, the velocities at each excitation frequency calculated in the harmonic analysis are exported from the green area in Fig. 1b and projected on a flat circular surface in order to act as a source in the acoustic domain.

2.2 Sound emission in fluid domain

To describe the emission and propagation of sound, the structural velocity must be related with the sound pressure at the interface. In the first step, the impedance is introduced. In the second step, the governing equations to

express this impedance term are reviewed and then applied in a third step to discretized structures, leading to matrix-over-node impedance expressions.

2.2.1 Impedance

In time-harmonic acoustics, the propagation of sound is described by the Helmholtz equation

$$\nabla^2 p(\mathbf{r}) + k^2 p(\mathbf{r}) = 0, \quad (4)$$

where p defines the pressure, $k = \omega/c$ the wave number, ω the angular frequency and c the speed of sound. By introducing the 3D free-space Green's function $G = \frac{1}{\|\mathbf{r} - \mathbf{r}'\|} e^{jk\|\mathbf{r} - \mathbf{r}'\|}$ with the receiver position $\mathbf{r} = (x, y, z)$ and the source at position $\mathbf{r}' = (x_s, y_s, z_s)$, the inhomogeneous spatial wave equation

$$(\nabla^2 + k^2)G(\mathbf{r}, \mathbf{r}') = 4\pi\delta(\mathbf{r} - \mathbf{r}'), \quad (5)$$

is satisfied for an unbounded medium external to the source [26], where $\delta(\mathbf{r} - \mathbf{r}')$ is the Dirac delta function representing the point source distribution. Combining Eq. (4) multiplied with $G(\mathbf{r}, \mathbf{r}')$ and Eq. (5) with $p(\mathbf{r}')$ and rearranging them leads to

$$\begin{aligned} \int_V [G(\mathbf{r}, \mathbf{r}') \nabla^2 p(\mathbf{r}') - p(\mathbf{r}') \nabla^2 G(\mathbf{r}, \mathbf{r}')] dV \\ = 4\pi \int_V p(\mathbf{r}') \delta(\mathbf{r} - \mathbf{r}') dV. \end{aligned} \quad (6)$$

Then applying the divergence theorem

$$C(\mathbf{r})p(\mathbf{r}) = \iint_{\Gamma} \left[p(\mathbf{r}') \frac{\partial G(\mathbf{r}, \mathbf{r}')}{\partial \mathbf{n}} - G(\mathbf{r}, \mathbf{r}') \frac{\partial p(\mathbf{r}')}{\partial \mathbf{n}} \right] dS(\mathbf{r}') \quad (7)$$

with

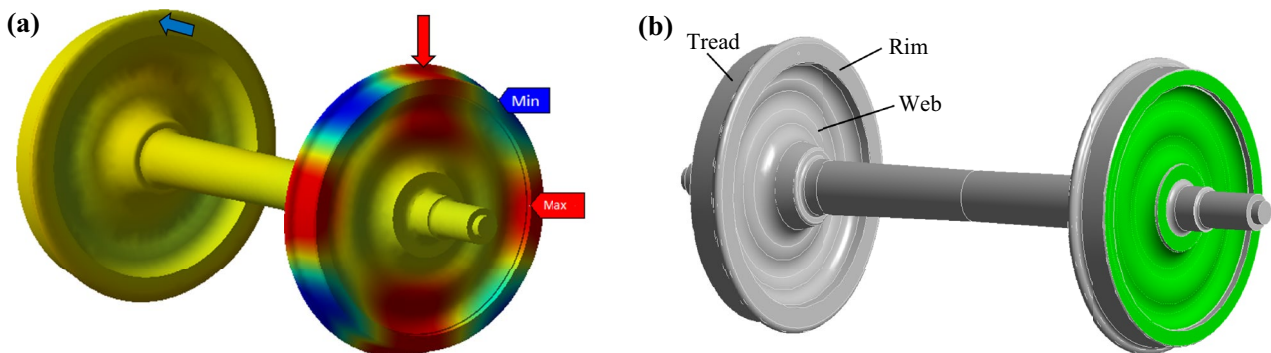


Fig. 1 Numerical model of railway wheelset DB97 for harmonic structural simulations: **a** vibrational mode shape of an excited wheel and location of the point source; **b** the geometry of the wheelset with the relevant surface (in green) acting as acoustic source

$$C(\mathbf{r}) = \begin{cases} 4\pi & \text{for } \mathbf{r} \in V, \mathbf{r} \notin S \\ 4\pi + \int_S \frac{\partial}{\partial \mathbf{n}} \frac{1}{R} dS & \text{for } \mathbf{r} \in V, \mathbf{r} \in S \\ 0 & \text{for } \mathbf{r} \notin V, \mathbf{r} \notin S \end{cases} \quad (8)$$

is obtained [27], where R is the distance $R = |\mathbf{r} - \mathbf{r}'|$, \mathbf{n} is the normal vector and S is a closed surface in the volume V . For the pressures on the surface, $C(\mathbf{r})$ is introduced, with a value equal to 2π for smooth surfaces. For the case of pressures within the same volume V , we can reformulate the equation to

$$p(\mathbf{r}) = \frac{1}{4\pi} \iint_{\Gamma} \left[p(\mathbf{r}') \frac{\partial G(\mathbf{r}, \mathbf{r}')}{\partial \mathbf{n}} - G(\mathbf{r}, \mathbf{r}') \frac{\partial p(\mathbf{r}')}{\partial \mathbf{n}} \right] dS(\mathbf{r}'), \quad (9)$$

which is used in a later step to derive the Rayleigh integral. Neglecting external forces, we obtain in linear acoustics

$$\frac{\partial p(\mathbf{r}')}{\partial \mathbf{n}} = -j\omega\rho\mathbf{v} \cdot \mathbf{n}, \quad (10)$$

which is used in the integral equation and therefore relates p and $\mathbf{v} \cdot \mathbf{n}$, the latter being known due to the continuity equation.

The numerical calculation of the impedance on vibrating structures requires their discretization. Three different frameworks are compared, as shown in Fig. 2. These are a baffled piston which represents a flat circular disk using the discrete calculation method (DCM) (Fig. 2a), the boundary element method (BEM) which represents a cylindrical surface (Fig. 2b) and the one-way fluid structure interaction in finite elements (FE) developed by using a cubic volume with cylindrical faces inside (Fig. 2c). The mesh of these models is shown in panels Fig. 2d–f. For the DCM, a grid with square elements is selected, see Fig. 2d. The BEM model consists of linear triangular surface elements (Fig. 2e), and

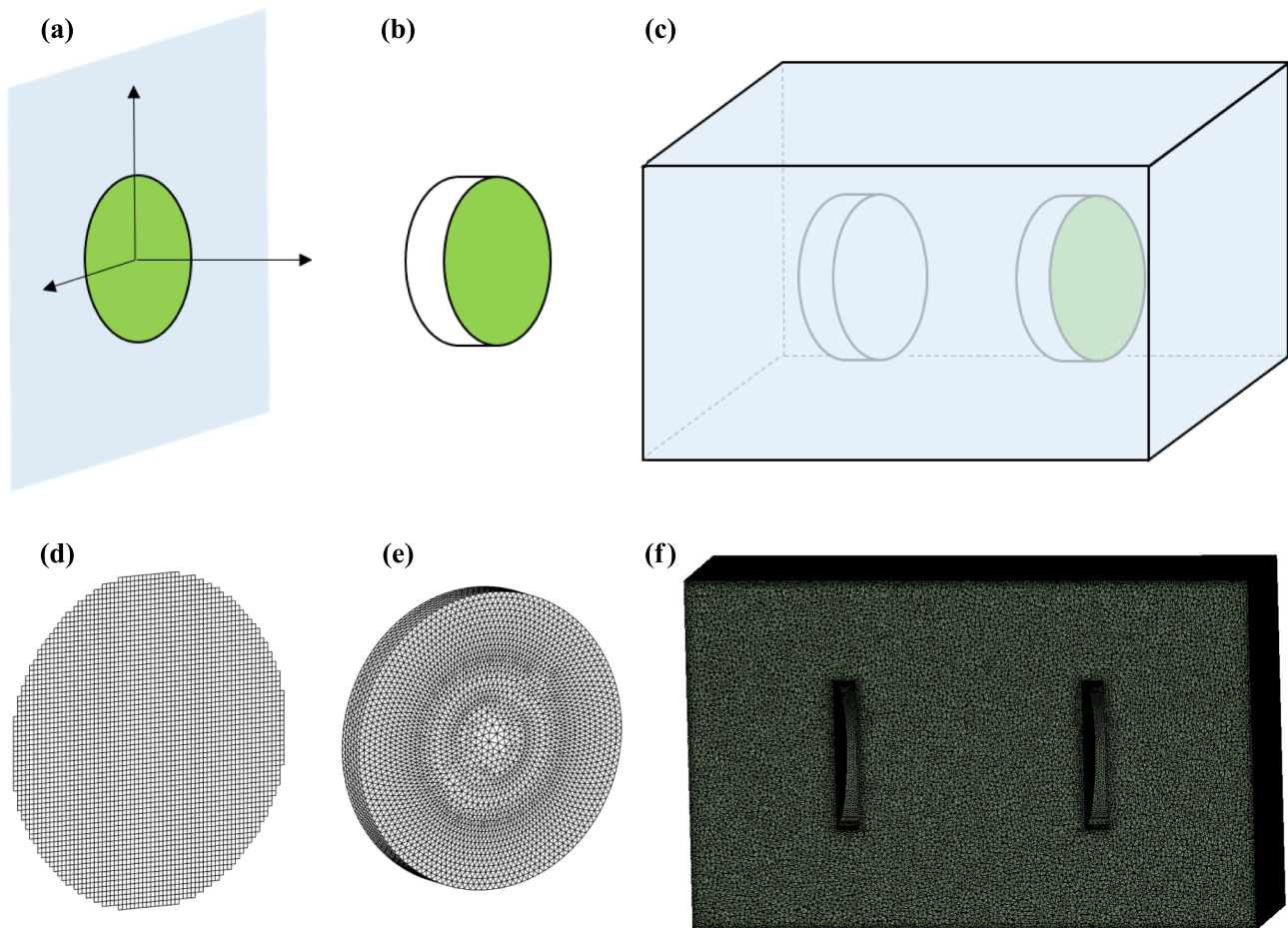


Fig. 2 The three investigated models and the corresponding meshes: **a** a circular piston mounted on an infinite rigid baffle, **b** a closed area for the boundary element method, **c** a finite element model with enclosure for the fluid domain, **d** the mesh of the discretized circular piston mounted on an infinite rigid baffle, **e** the closed surface mesh for the boundary element method, and **f** the mesh of the finite element model for the fluid domain

the FEM model is composed of tetrahedral elements of quadratic order (Fig. 2f). The maximum element size for each model is 0.01 m.

For discretized bodies, an acoustic impedance matrix $\hat{\mathbf{Z}}$ is necessary to describe the relation between pressure and velocity. In the following, for all three models, which are based on different discretization schemes, the velocity field \mathbf{v}_Γ from the harmonic structural simulation is used as a sound source to calculate the sound pressure of this sound source \mathbf{p}_Γ on the input surface Γ .

$$\mathbf{p}_\Gamma = \hat{\mathbf{Z}}\mathbf{v}_\Gamma. \quad (11)$$

Since each model is subject of different discretization methods, the differences in the calculation of the impedance matrix will be discussed in the following sections. The velocities of each frequency extracted in the harmonic analysis are now projected on the green surface for a baffled piston, a closed cylinder volume and a closed cylinder inside a box filled with a fluid. After calculating the impedance on the corresponding surfaces, the sound propagation in space can be further calculated by using the retrieved surface pressure \mathbf{p}_Γ .

2.2.2 Boundary element method

The boundary element method is based on a closed structure that is discretized on its surface. In order to calculate the surface pressures, Eq. (7) follows the discretized form [19, 27]

$$C\mathbf{p}_\Gamma = \hat{\mathbf{A}}\mathbf{p}_\Gamma - \hat{\mathbf{B}}\mathbf{v}_\Gamma, \quad (12)$$

with $A_{kl} = \frac{\partial G(\mathbf{r}_k, \mathbf{r}_l)}{\partial n} s_k$ and $B_{kl} = j\omega\rho G(\mathbf{r}_k, \mathbf{r}_l) s_k$ being entries of matrices $\hat{\mathbf{A}}$ and $\hat{\mathbf{B}}$, respectively, where G is the Green's function and k and l are the elements on the vibrating surface; \mathbf{r}_k and \mathbf{r}_l are the spatial coordinates of the receiving and emitting points and s_k is the surface area; and C is the geometric quantity of the surface angle, which is generally 2π for continuous surfaces. By including the geometric surface properties, BEM takes radiation effects of edges and therefore the realistic boundary conditions into account.

For stability and robustness, the BE method used in this article considers the combined Helmholtz integral equation formulation (CHIEF). In [19], the authors use the CHIEF so that more complex geometries with complex meshes can be treated and the uniqueness problem is solved by introducing additional points, leading to an over-determined system that is solvable

$$\mathbf{p}_\Gamma = (\hat{\mathbf{A}} - \hat{\mathbf{C}}\hat{\mathbf{I}})^{-1} \hat{\mathbf{B}}\mathbf{v}_\Gamma. \quad (13)$$

where $\hat{\mathbf{I}}$ is the identity matrix. Finally, using the obtained pressure on the surface \mathbf{p}_Γ , one can calculate the pressure in

receiver points \mathbf{p}_{rec} within the fluid volume V using $C = 4\pi$, according to Eq. (8),

$$C\mathbf{p}_{\text{rec}} = \hat{\mathbf{A}}\mathbf{p}_\Gamma + \hat{\mathbf{B}}\mathbf{v}_\Gamma. \quad (14)$$

2.2.3 Baffled piston model

The case of a piston mounted on an infinite rigid baffle can be derived in the frequency and time domain [28]. In this work, the expression for the acoustic pressure of a baffle is derived using the Kirchhoff–Helmholtz integral theorem Eq. (9) in the frequency domain describing the sound pressures within a volume free of sources, where sound pressures and velocity are prescribed in all points on any surface. Since a baffle is a vibrating surface mounted on an infinite rigid wall, the method of images is used in the Green's function considering two acoustic sources

$$G = \underbrace{\frac{e^{jkR}}{R}}_{\text{Source}} + \underbrace{\frac{e^{jkR'}}{R'}}_{\text{Image source}}, \quad (15)$$

where $R = \sqrt{(x - x_s)^2 + (y - y_s)^2 + (z - z_s)^2}$ and $R' = \sqrt{(x - x_s)^2 + (y - y_s)^2 + (z + z_s)^2}$ are the distances between receiver and the source and receiver and the image source, respectively, with the receiver position $\mathbf{r} = (x, y, z)$ and source at position $\mathbf{r}' = (x_s, y_s, z_s)$. Since the sources are on the wall $z = 0$, the second term of the Green's function on the surface becomes due to the infinitely small disk (equivalent to $R = R'$)

$$G(z = 0) = \frac{2}{R} e^{jkR}, \quad (16)$$

and since the normal vector is perpendicular to the flat surface, $\nabla_s G \cdot \mathbf{n}_s$ vanishes in normal direction. Due to Euler equation for the gradient of the pressure we obtain the Rayleigh integral [28]:

$$p = -\frac{j\omega\rho}{2\pi} \iint \frac{v}{R} e^{jkR} dS, \quad (17)$$

where ρ represents the density of the fluid. Since this equation is only valid for constant velocities over the vibrating surface, a varying velocity field on the surface is not possible and therefore a discretization of the surface is needed. To deal with this issue, Hashimoto introduced the DCM [24]. It expresses the radiation impedance of a vibrating piston on an infinite planar baffle. The impedance is calculated from two parts: the self-radiation impedance describing the impact of the velocity on the pressure of the same element, see Fig. 3a, and the mutual radiation impedance describing the impact of the velocities of all interacting elements except the

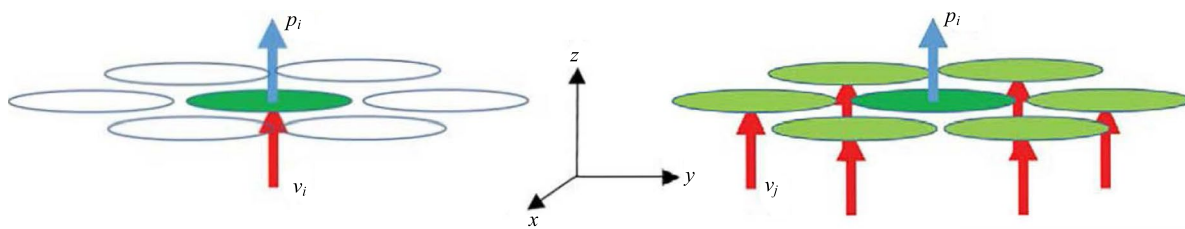


Fig. 3 The schematic view of **a** the self-radiation impedance and **b** the mutual radiation impedance

one of the element itself on the pressure, see panel (b). The application and validation of the DCM method can be found in several publications [25, 29].

For the DCM, the baffled piston is discretized into square elements with length Δx , see Fig. 4a. Each of the elements can be approximated by disks (Fig. 4b) that can be treated as small pistons with an equivalent radius $a = \sqrt{\frac{\Delta x^2}{\pi}}$ and surface area S . Their interaction is calculated to the corresponding distance d between the center of each circle.

The self-radiation impedance is originally derived from the Rayleigh integral [30]. It is valid for the entire frequency domain and can be found in textbooks such as [28, 31]. A vast body of literature is available on deriving asymptotic and series expansion solutions for special cases of the Rayleigh integral for circular [22, 32] as well as for rectangular plates [33]. Two very interesting cases are the axial pressure ($\theta = 0$) and far-field pressure ($r \gg a$) for all θ mentioned in [28]. In this work, we describe the relationship between pressure and velocity derived from the mechanical radiation impedance Z_m , which relates to the relationship between force and velocity:

$$Z_m = \frac{f}{v_n} = \frac{\int_S p dS}{v_n} = \frac{\int_S \frac{-j\omega\rho}{2\pi} \int_S \frac{v_n}{R} e^{jkR} dS dS}{v_n} \quad (18)$$

$$= \int_S \frac{-j\omega\rho}{2\pi} \int_S \frac{e^{jkR}}{R} dS dS,$$

where f is the force and v_n is the velocity. This complex integral is solved in [28] to

$$Z_m = R_r + jX_r = \rho c S [R_1(2ka) + jX_1(2ka)] \quad (19)$$

with

$$R_1 = 1 - \frac{2J_1(2ka)}{2ka} \quad (20)$$

and

$$X_1 = \frac{2S_1(2ka)}{2ka}, \quad (21)$$

which results in the analytical formula for the self-radiation impedance:

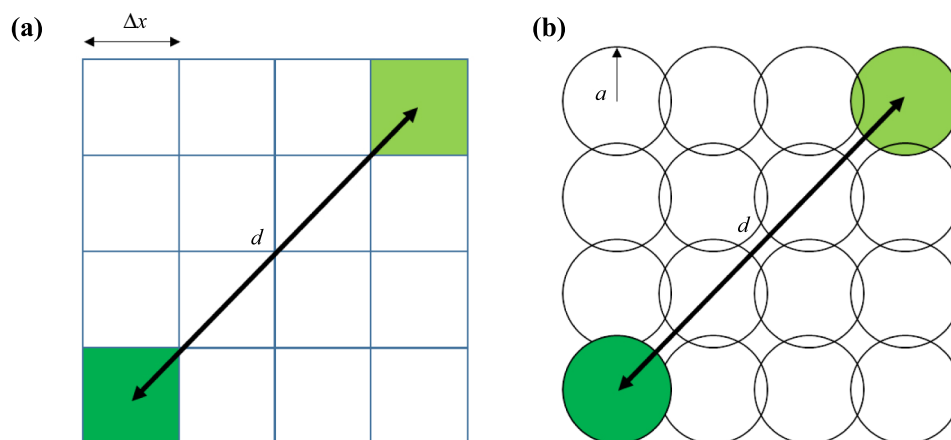


Fig. 4 Illustration of discretized elements interaction in the DCM: **a** a grid of square elements that is suitable for the DCM method and **b** the square mesh approximated in DCM by as many circular pistons interacting with each other. a is the radius of one baffle and d the distance of between the center of two baffles. Δx defines the side length of a square element

$$Z_{m_{\alpha\alpha}} = \rho c S \left(1 - \frac{J_1(2ka)}{ka} + j \frac{S_1(2ka)}{ka} \right), \quad (22)$$

where c is the speed of sound in air, J_1 is the Bessel function of first kind and S_1 is the Struve function of first kind. The relation between the pressure p_α and velocity v_α at one specific baffled piston is called the acoustic impedance $Z_{\alpha\alpha}$:

$$Z_{\alpha\alpha} = \frac{p_\alpha}{v_{n,\alpha}} = \frac{Z_{m_{\alpha\alpha}}}{S} = \rho c \left(1 - \frac{J_1(2ka)}{ka} + j \frac{S_1(2ka)}{ka} \right). \quad (23)$$

The expression of the mutual radiation impedance mentioned in the DCM can be found in [22] for interactions of circular pistons of arbitrary size and spacing. It is derived by taking the far-field solution of the pressure field of a baffled piston. As derived in the transient analysis of [22], the time-dependent pressure $p(x, \tau)$ can be expressed as a convolutional integral of the time-dependent velocity of the j th piston v_j and the piston's impulse response $h(x, \tau)$:

$$p(x, \tau) = \rho c \frac{\partial}{\partial \tau} \int_0^\tau h(x, u) v_j(\tau - u) du. \quad (24)$$

From this, we obtain the far-field expression for the pressure velocity relation caused by the interaction of element α and element β :

$$Z_{\alpha\beta} = j \rho c k a S \frac{e^{-jkd}}{2\pi d} \left(\frac{2J_1(ka)}{ka} \right)^2, \quad (25)$$

with d considering the distance between α and β .

By using the expressions for the self-radiation and mutual radiation impedance (i.e., Eqs. (23) and (25), respectively), one can now calculate the pressure on the interface Γ as described in Eq. (11). The propagation of sound in the acoustic domain is then achieved in the same way as in Eq. (14).

2.2.4 Finite element method

The one-way coupling of a fluid–structure interaction problem in the frequency domain is described by the following equations [34]:

$$\begin{bmatrix} -\omega^2 \begin{bmatrix} \hat{M}_S & 0 \\ \rho_0 \hat{R}^T & \hat{M}_F \end{bmatrix} - j\omega \begin{bmatrix} \hat{C}_S & 0 \\ 0 & \hat{C}_F \end{bmatrix} + \begin{bmatrix} \hat{K}_S & -\hat{R} \\ 0 & \hat{K}_F \end{bmatrix} \end{bmatrix} \begin{Bmatrix} u \\ p \end{Bmatrix} = \begin{Bmatrix} f_S \\ f_F \end{Bmatrix}. \quad (26)$$

where \hat{M}_S and \hat{M}_F are the mass matrices of solid and fluid, \hat{C}_S and \hat{C}_F are the corresponding damping matrices, and \hat{K}_S and \hat{K}_F the corresponding stiffness matrices; \hat{R} is the coupling matrix between fluid and solid domain; u and p are the degrees of freedom of displacement and pressures,

respectively; f_S and f_F represent the external forces acting on the fluid and solid domain; ρ_0 is the density of the fluid.

The problem in the fluid domain can then be rewritten as

$$-\omega^2 \rho_0 \hat{R}^T u + [-\omega^2 \hat{M}_F - j\omega \hat{C}_F + \hat{K}_F] p = 0, \quad (27)$$

since the force on the fluid f_F is zero. From that, the equations for the surface pressure can be expressed by the following equation

$$p = [-\omega^2 \hat{M}_F - j\omega \hat{C}_F + \hat{K}_F]^{-1} \omega^2 \rho_0 \hat{R} u, \quad (28)$$

where

$$p = \hat{Z} v = -\hat{Z} j \omega u \quad (29)$$

leads to the impedance matrix

$$\hat{Z} = [-\omega^2 \hat{M}_F - j\omega \hat{C}_F + \hat{K}_F]^{-1} (j \omega \rho_0 \hat{R}). \quad (30)$$

Summarizing the three models, the baffled piston and BEM propagate in space with Green's function and the closed surface model solves spatial pressures and the surface pressures all at once. In comparison to the boundary element method, the discrete calculation method treats the impedance of an infinite baffled piston, describing the velocities on an infinite plane without any discontinuities such as sharp edges. In contrast, the BEM and also the FEM for fluid–structure interaction capture these scattering effects.

3 Vibrational measurements and simulation

To validate the numerical models, two different measurements are performed. At first, a typical freight train wheel of the type DB97, that has been in operation and is therefore worn, is excited in the axial direction with an electrodynamic shaker (TIRA—TV 51120) to measure the velocities in axial direction. The input force is measured with a force sensor (PCB 208C01) and the velocity by a SWIR scanning laser Doppler vibrometer (Optomet). The measurement is taken at a sampling rate of 40,000 Hz. The wheelset has a radius of 0.47 m and is part of a wheelset with a total weight of 960 kg. To approximate free boundary conditions, two rubber blocks are placed between the axle of the wheelset and the supporting wooden pallet.

The numerical model is built in Ansys. The mesh of the steel wheel in the structural domain consists of tetrahedral elements of quadratic order with a maximum element size of 0.02 m. The Young's modulus is 210 GPa, the Poisson's ratio is 0.3, and the density is 7850 kg/m³. The entire mesh consists of 98,000 elements. Structural damping is not considered in this model, which in theory leads to infinite magnitude at the resonances and is only finite due to the chosen

frequency sampling. The geometry is based on a technical drawing of a standard wheelset that is not worn, meaning differences between experiment and geometry exist.

In the frequency response function of Fig. 5, the comparison between the harmonic FEM model and the measurements is shown. The frequencies, their mobility values, and the width of the peaks agree very well between the experiment and simulation. The error between the modal frequencies is less than 5% for the frequency range up to 3000 Hz. The mode shapes are shown at several frequency peaks. The accurate prediction of the vibrational velocity magnitude and pattern is important, as they are the ultimate source of sound.

4 Validation of radiation models with lab measurements

In this section, the results predicted by the three acoustic models are presented. They are put into practice with different software tools. The BEM model is realized by using the OpenBEM code of Ref. [19]. The baffled piston model is implemented in MATLAB, and the FEM is implemented with the use of Ansys [34]. To reduce the complexity, the agreement between the three models is first investigated in a free-field environment without any reflective surfaces. The modeled velocity profiles obtained in the previous chapter serve as input for the acoustic radiation models. Subsequently, acoustic

measurements are used to validate the models. Due to the existing facilities for measurements, reflective surfaces must now be included in the numerical calculations.

4.1 Acoustic free-field radiation

As mentioned in the Sect. 2, the front surface of the wheel is the excitation source and the interface between the structural and fluid domain. The green area in Fig. 6a represents the surface where the fluid–structure interaction occurs (contributions from the axle and other surfaces are assumed negligible with respect to the frontal emission of the single wheel). The impedance matrix \hat{Z} is evaluated as mentioned in Sect. 2.2.1 to obtain the surface pressure p_Γ from the normal velocities v_n . Due to the different meshes (triangular elements for BEM, quadrilateral for the baffled piston and tetrahedrons for FEM), a direct comparison of the impedance matrix would be cumbersome. Therefore the pressure distribution along the marked line is shown for selected modes.

To evaluate the acoustic model, we compare the pressures on the source itself and on a surface that is some distance (0.88 m) away from the source. This is mainly dictated by the computational feasibility of the FE model, where the surface at that distance is at the border of the FE enclosure. The enclosure must be large enough to absorb outgoing waves properly and small enough so that computational feasibility is still guaranteed using an impedance boundary. This means that for the valid frequency range, the distance of the absorption boundary must be at least one half of the largest

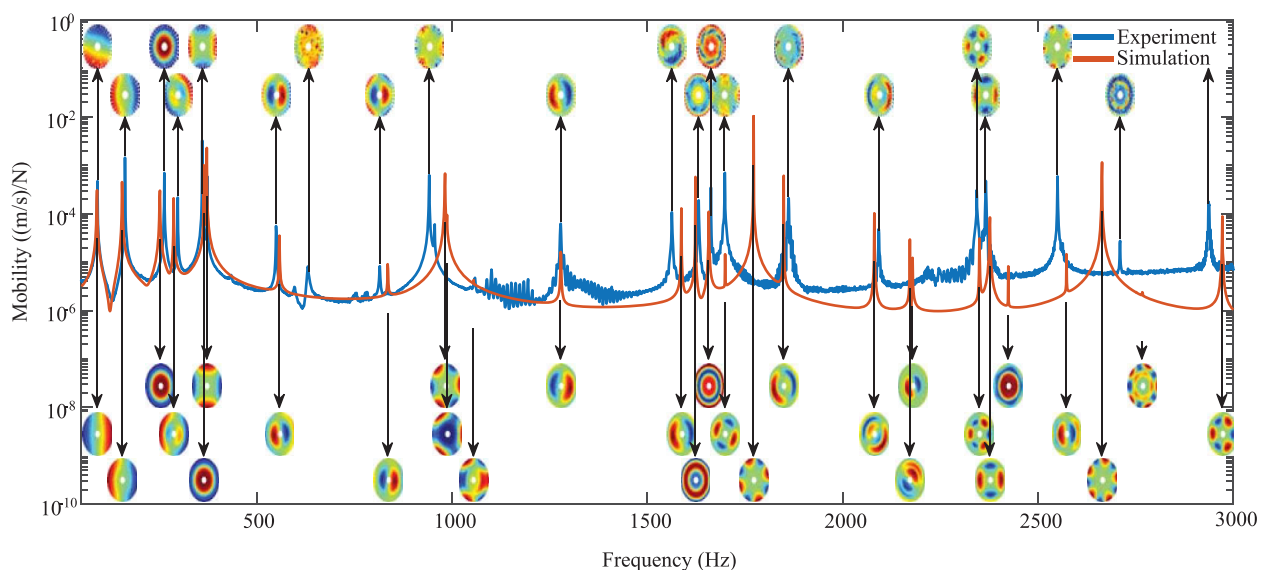


Fig. 5 Average (of absolute values) mobility in axial direction with visualized mode shapes at frequency peaks

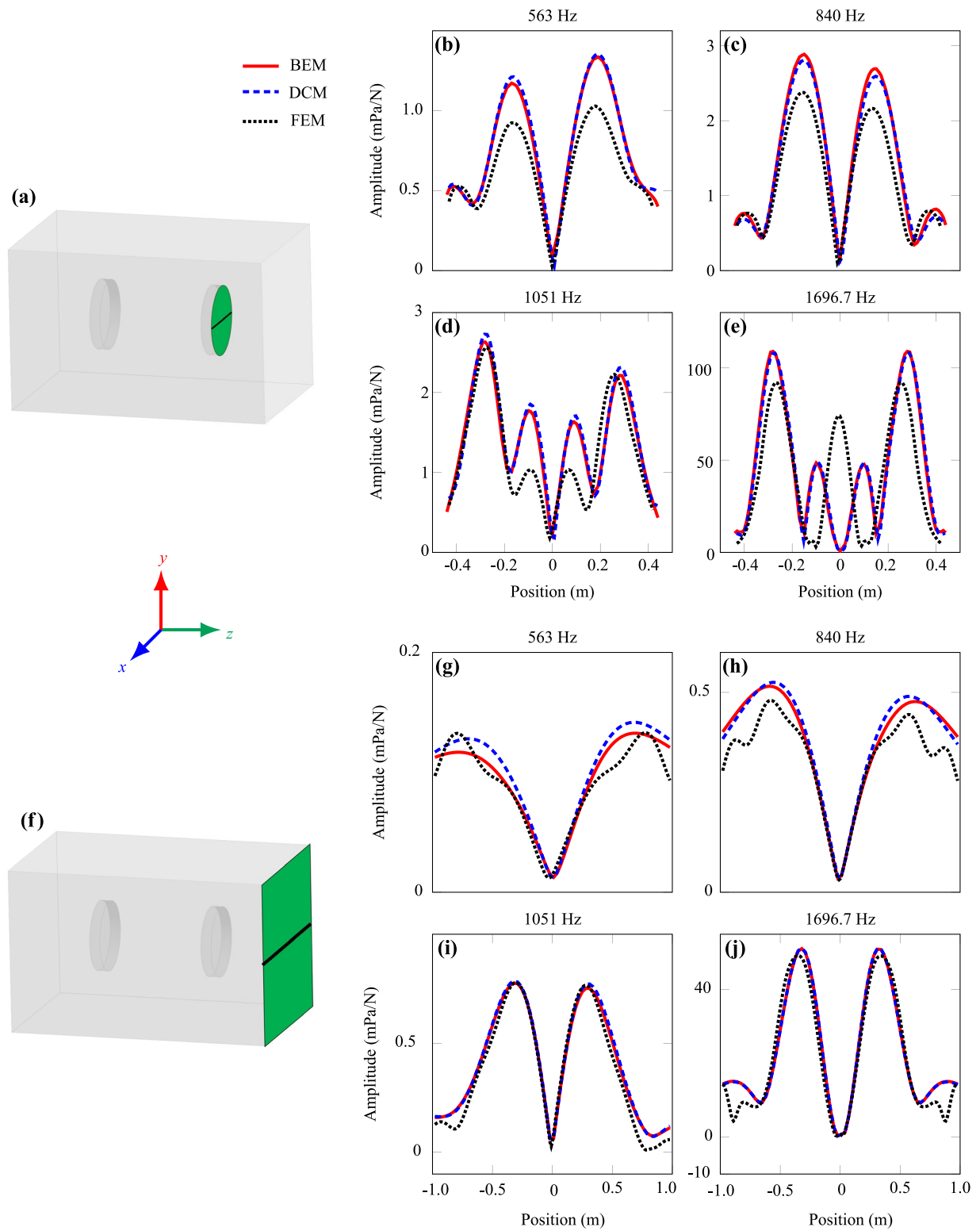


Fig. 6 Sound pressure per unit force comparison between BEM, DCM and FEM. Selected peak frequencies of the FRF (explained in Fig. 5) are evaluated on the black line for the emitting surface **a** and receiving surface **f**, where **b–e** correspond to configuration **a** and **g–j** correspond to **f**

wavelength away from the source and the elements of the air must be meshed at least with six elements per wavelength of the highest frequency to avoid numerical instability using linear shape functions [35]. The modes on the emitting surface are evaluated at the black line in Fig. 6a. The pressures obtained from the baffled piston and the boundary element models are in very good agreement, see panels Fig. 6b–e. The finite element model gives more divergent results; this is well known in research as the enclosure in a finite volume faces several difficulties, such as boundary conditions at infinity (in our case we use absorption boundaries in Ansys) and mesh size of the elements, which limits the range of valid frequencies (in our case from 200–2000 Hz). The comparison looks even better when we evaluate the pressure on a line on the surface 0.88 m away from the source, see Fig. 6f. In panels Fig. 6g–j, they show very good agreement between baffled piston and BEM, and slightly varying results in FEM, due to boundary condition effects.

4.2 Ground effect considerations for acoustic model validation

We compared in Sect. 4.1 the three methods BEM, DCM and FEM in free-space conditions and observed a very good agreement, especially between BEM and DCM. Now we introduce more applicable conditions where ground reflections are considered. Since FEM is computationally too expensive to compare it further away with experiments, we focus on the BEM and the discretized baffled piston.

4.2.1 Experimental setup

The experiment is realized in a hall with a height of 10 m and a concrete floor. The same railway wheel as mentioned in the vibrometric experiment is used and excited 20 cm above the floor (wheel center at a height of 0.68 m). This time we use a hammer instead of the shaker, since the shaker itself emits a significant noise level which interferes with the acoustic radiation of the wheel. Excitation is done in axial direction with the hammer of type PCB-086C03, which has a plastic tip for low frequencies (50–1000 Hz) and a steel tip for frequencies in the range from 1000 to 5000 Hz. We construct a beam with two supports where 9 microphones (B&K 4189) are mounted on and equally spaced every 0.2 m, see Fig. 7. With this configuration, we can measure the sound emission from the excited railway wheel at different heights and also shift the array of microphones 0.1 m to get a grid with finer resolution. This setup enables measurements of directivity. Measurements are conducted with LabVIEW using NI PXIe-1071 and PXI-4498 for a measurement time between 2 and 4 s for the hammer using a sampling rate of 25,000 Hz.



Fig. 7 Experimental setup for sound emission

4.2.2 Results

In order to make a valid comparison between experiments and simulations, ground effects are taken into account by introducing a term for the image source within Green's function, the so-called half-space assumption. As described in [36], the expression for the Green's function can be described in more general terms as

$$G(\mathbf{r}, \mathbf{r}') = \frac{e^{ikR}}{R} + R_1 \frac{e^{ikR'}}{R'}, \quad (31)$$

where $R_1 = 0$ for an infinite space and $R_1 = 1$ for a semi-infinite hard boundary space. If the reflecting plane is the xz -plane, then $R = \sqrt{(x - x_s)^2 + (y - y_s)^2 + (z - z_s)^2}$ and $R' = \sqrt{(x - x_s)^2 + (y + y_s)^2 + (z - z_s)^2}$ are the distances between receiver and the source and receiver and the image source, respectively, with the receiver position $\mathbf{r} = (x, y, z)$ and source at position $\mathbf{r}' = (x_s, y_s, z_s)$. The half-space assumption is equivalent to a mirrored, virtual second source leading to the hard boundary condition of

$$\mathbf{v}(\mathbf{r}_{\text{rp}}) \cdot \mathbf{n}_{\text{rp}} = 0, \quad (32)$$

which considers normal velocities equal to zero at the reflecting plane with coordinates \mathbf{r}_{rp} and normal vector \mathbf{n}_{rp} . Since the setup is built on a flat concrete floor, a reflection coefficient R_1 equal to one is a valid approximation. In a first analysis, the frequency response of the baffled piston, the BEM method and the experiment is obtained at a distance of 2 m away from the wheel at a height of 1.5 m. The points are spaced equally every 0.2 m from 0.8 to −0.8 m along that line. The averaged value over the number of points per frequency is displayed for each method in Fig. 8. This shows that the peaks of the experiment (both magnitude and frequency) are

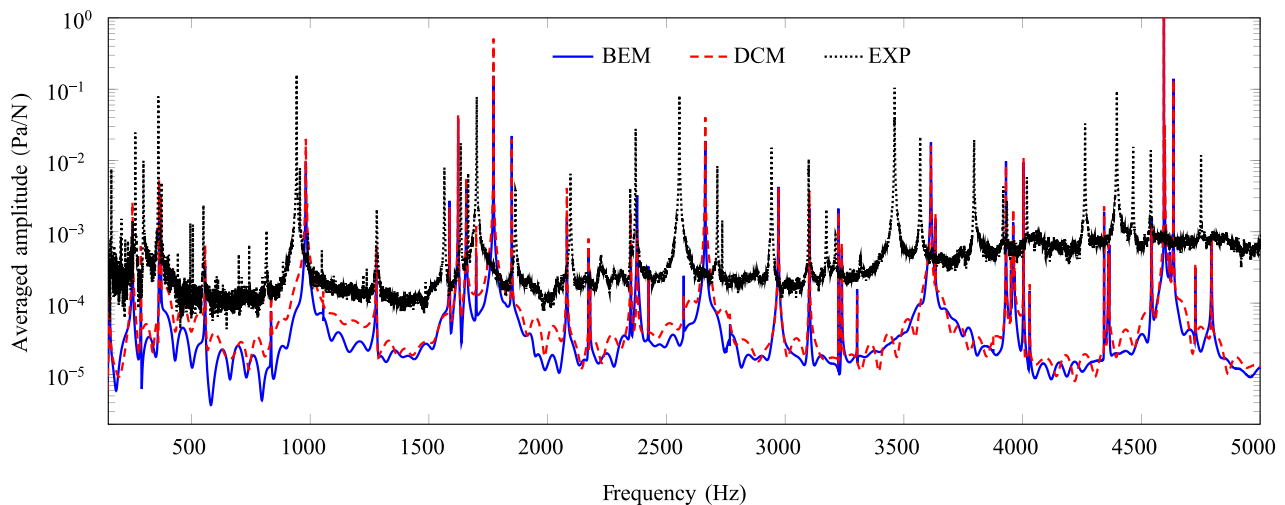


Fig. 8 Averaged frequency response of the sound pressure normalized by the excitation force, using nine receiver points

well captured by the simulation models. The overall noise floor of the experiment exceeds the simulation on a constant level, which is a common effect due to background noise which can be only eliminated in anechoic rooms. Despite the use of absorbing materials and measuring in a large hall, reflections are inevitable and perfect amplitude matching therefore not possible. The reflections do not affect the frequency of the modal peaks and therefore it is still possible to identify them. As can be seen in Fig. 5, the shift between numerical model and experiment is increasing with frequency. Since the vibrational response serves as input for the acoustic model the shift in frequency is transferred to the acoustic domain. In order to get a better fit between simulation and experiment, an intensive measurement of the wheel geometry is necessary, since changes in mass and radius due to wear alter the results. Further uncertainty is introduced by the Young's Modulus of the steel which can vary between 190 and 210 GPa.

One can recognize differences between BEM and DCM due to ground effects. This is caused by the different assumptions of these methods. The comparison can be seen more closely when visualizing the modes on a surface 2 m distance away with a width of 2.1 m, see Fig. 9. The vertical direction describes the height starting at the bottom of the concrete floor. Three resonance frequencies are selected and the occurring mode shapes are compared by including the half-space Green's function. Although the difference in magnitude is varying, it is possible to clearly identify the normalized modes visually for DCM and BEM and compare them to experiments. The visual agreement of the last mode between simulation (Fig. 9i, j) and experiment (Fig. 9k) is unsatisfactory because the resolution of the experiment cannot reflect the level of detail of the emission pattern.

We separate the modes into two categories: “baffled” and “unbaffled” modes. We refer to a baffled mode shape when the outer rim of the wheel experiences significantly less vibration compared to the inner surface, leading to dominant emission from the wheel web and negligible edge radiation effects at the edges. One of these baffled mode shapes can be seen in Fig. 9h at 1623 Hz. The corresponding acoustic emission calculated with DCM (see Fig. 9e) excellently agrees in terms of emission pattern to the BEM and experimental counterparts (Fig. 9e, f, respectively). Even the unbaffled modes (Fig. 9d, l), where the rim experiences strong vibrations compared to the web, feature very similar acoustic radiation patterns (cf. Fig. 9a–c and i–k).

Figure 9 shows a good *qualitative* comparison of the prediction methods with experiments. Specifically, the predicted waveforms are consistent with each other and to the available experimental results. Regarding the latter, it should be pointed out that the resolution is not enough for the high frequency mode (Fig. 9k). In the following, we would like to *quantitatively* compare the acoustic prediction methods associated with the baffled and unbaffled modes in Fig. 9d, h and l.

Therefore, we look in Fig. 10 at the emission patterns of the modes with DCM and BEM and disregard the experiments. We present simply the magnitude and directionality along one circular line with a radius of 2 m between -60° and 60° at different heights (0.1, 0.65 and 1.9 m). For the baffled mode at 1623 Hz, the agreement is excellent in front of the wheel (Fig. 10e) and slightly varying close to the floor (Fig. 10d) and at a large angle of 70° at 1.9 m (Fig. 10f), where even small edge radiation effects are dominating the wheel emission patterns and the assumption of the baffled

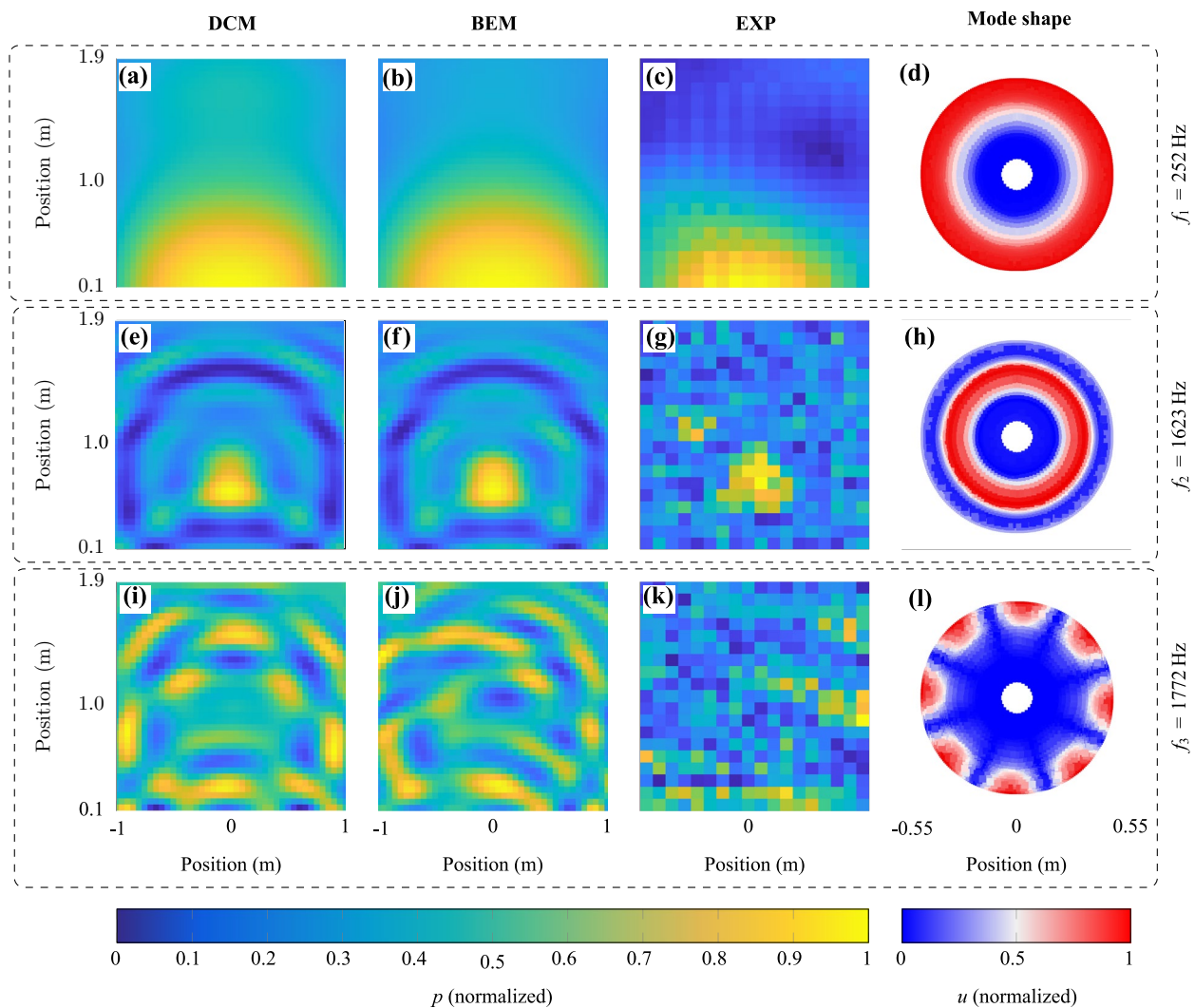


Fig. 9 Emission patterns caused by the corresponding mode shape in 2.0 m distance away from the wheel surface going from 0.1 m to 1.9 m height. In the first (a, e, i), second (b, f, j) and fourth (d, h, l) column, the results from simulation are shown at the frequency f_n with $n = \{1, 2, 3\}$. The third column (c, g, k) illustrates the experimental results, caused at slightly varying frequencies ($f_1 = 263.75$ Hz, $f_2 = 1634$ Hz and $f_3 = 1701.25$ Hz). The modes are normalized with respect to their physical quantity. The pressures (columns 1–3) $[p_{\min}, p_{\max}]$ and the displacements $[u_{\min}, u_{\max}]$ (column 4) of each mode map to the interval $[0, 1]$

piston does not take into account the pressure distribution on the side of the wheels. For the un baffled mode shapes, Fig. 10a–c shows that the directionality is well captured for the mode at 252 Hz but the magnitude is varying a lot, which is caused by the half-space assumption in DCM. The reason why the agreement of directionality is that good lies in the nature of its ring shape. For the un baffled mode shape with strong directionality contributions due to four nodal lines at 1772 Hz, one can witness at all three heights that neither the magnitude nor the directionality pattern can be meet between the two DCM and BEM.

Finally, in order to highlight the edge radiation effect, leading to the different results of the baffled wheel mode

at 1623 Hz and the un baffled wheel mode at 1772 Hz, we perform the numerical experiment described in Fig. 11a. We consider a receiver surface (black) close to the reflective hard boundary (gray), to see how the waves propagate in axial directions away from the wheel. We investigate here only DCM and BEM. For the baffled mode shape, the emission pattern between DCM (Fig. 11b) and BEM (Fig. 11d) agrees very well whereas for the un baffled mode shape the edge radiation reveals clear discrepancies between DCM (Fig. 11c) and BEM (Fig. 11e). These are especially visible close to the wheel (left) and close to the reflecting surface (bottom). This clearly highlights the limitations of the DCM.

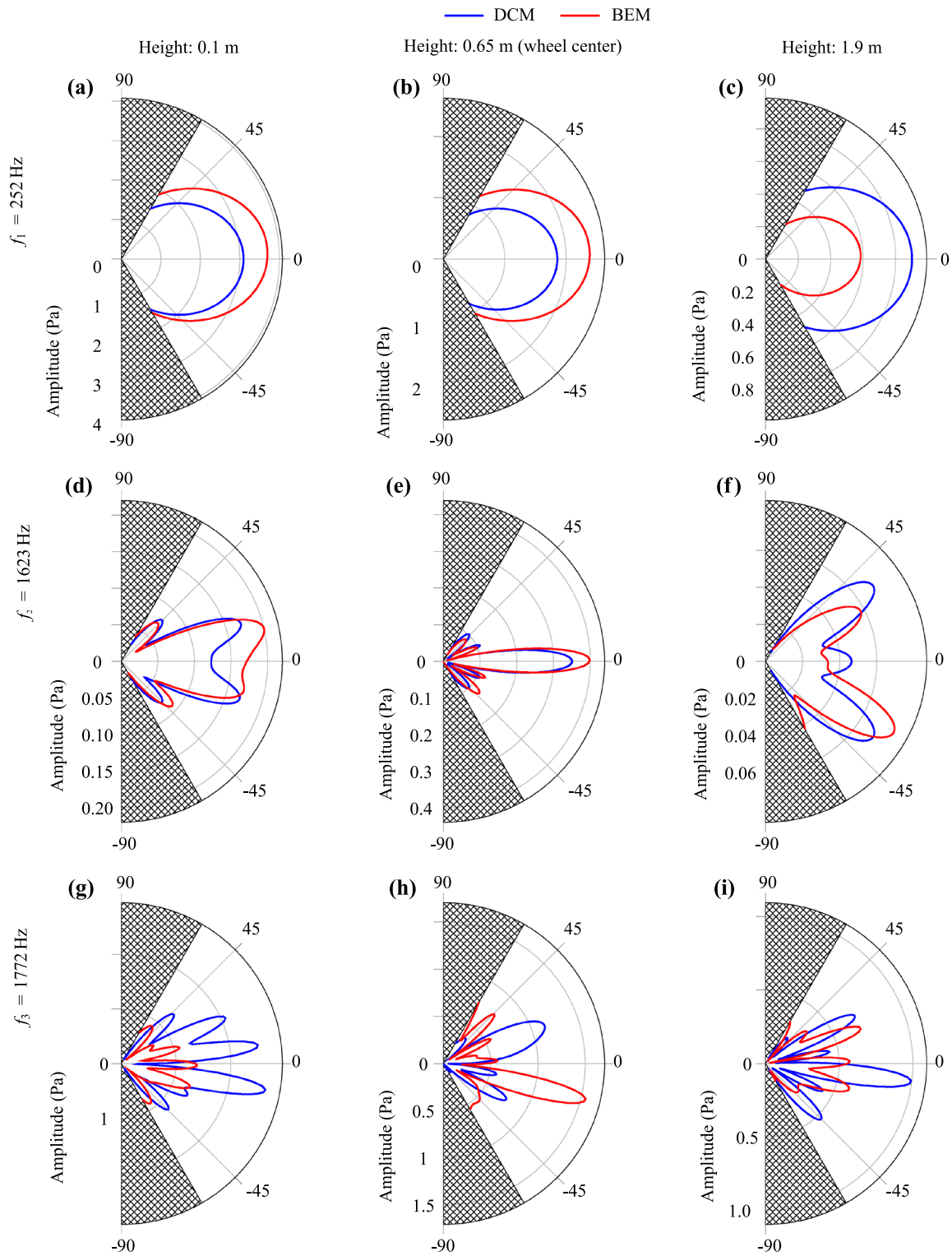


Fig. 10 Polar plots of the mode shapes presented in Fig. 9 showing the directionality along a line in 2.0 m distance away from the wheel surface corresponding to a height of 0.1 m (a, d, g), 0.65 m (b, e, h) and 1.9 m (c, f, i). The results from simulation are shown at the frequency f_n with $n = \{1, 2, 3\}$

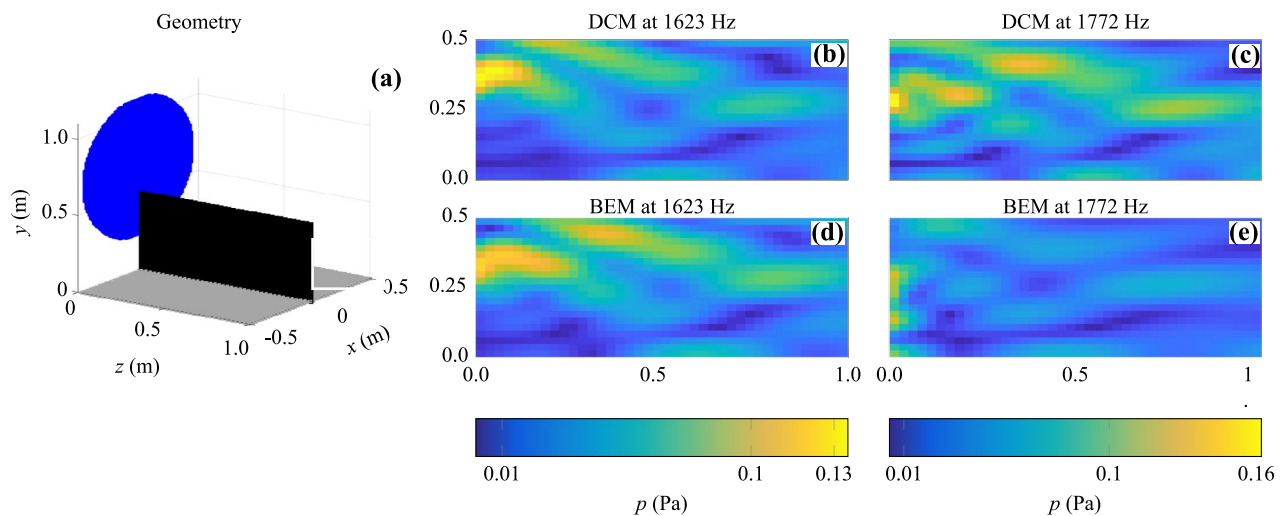


Fig. 11 Comparison of edge radiation effects: **a** schematic view of receiver surface (black) close to the reflective hard boundary (gray); **b, d** baffled mode shape such as seen in Fig. 9 at 1623 Hz that can be well captured with DCM and BEM since edge radiation effects are not dominant; **c, e** unbaffled mode shapes such as seen in Fig. 9 at 1772 Hz that lead to strong edge radiation effects at the edges of the wheel and are dominant compared to baffled effects. A hard-space boundary condition considerably changes the results in the near field for unbaffled wheel modes



Fig. 12 Wheelset with roller bearings used for experiments

4.3 Axle and effects on acoustic emission

In the previous sections, the results are shown using the normal velocities of the frontal surface of a wheelset. To better understand the importance of an entire wheelset, we investigate two different wheel geometries (single wheel and wheelset) and the boundary conditions. For experimental comparison, we introduce a standard passenger train wheelset with a radius of 0.48 m and a mass of 850 kg. The axle is equipped with two bearings, each weighing 60 kg, see Fig. 12.

In Fig. 13c, we compare the experimental results of the above mentioned wheelset with attached bearings to a single wheel using FEM without axle and fixed at the axis of symmetry by including a small hole with a diameter of 1 cm (illustrated in Fig. 13a). This was motivated by the work

of [15], where the axisymmetric cross section of a single wheel is fixed at the axis of symmetry. With the exception of applying radial excitation instead of axial, the setup aligns with the one illustrated in Fig. 5. This reveals the strength of numerical modeling for investigation of different excitation profiles, since the force on the wheel consists of both axial and radial contributions. This comparison shows missing modes at low frequencies and additional modes not corresponding to the experimental setup. A minor frequency deviation is observable at the higher frequency range. Figure 13d compares the entire wheelset using FEA without supports to the experiments, also revealing differing modes at incorrect frequencies. By incorporating springs with stiffnesses of 700 MN/m, dampers with damping of 518 kNs/m and a connected point mass (60 kg) approximating stiffness, friction and weight of roller bearings (illustrated in Fig. 13b), the results closely align with experimental data, see Fig. 13e. This finding strongly supports the notion that the axle and its boundary conditions play a critical role in the sound emission of railway wheels. As described in [13], the axle influences especially the modes with harmonic indices $n = 0$ (extension of the axle) and $n = 1$ (flexure of the axle). This leads to especially strong impact of the axle at frequencies between 150 and 1500 Hz, see Fig. 14.

Using harmonic FE simulations as input, the differences are also apparent when using BEM with results projected onto a cylinder, see Fig. 14a. The results of the pressure in a point 7.5 m away and in 1.2 m height are shown. Notably, between 150 and 1500 Hz, the frequencies of the modes vary significantly. While one could argue that radiation efficiency from railway wheels is less significant in this range, an exact

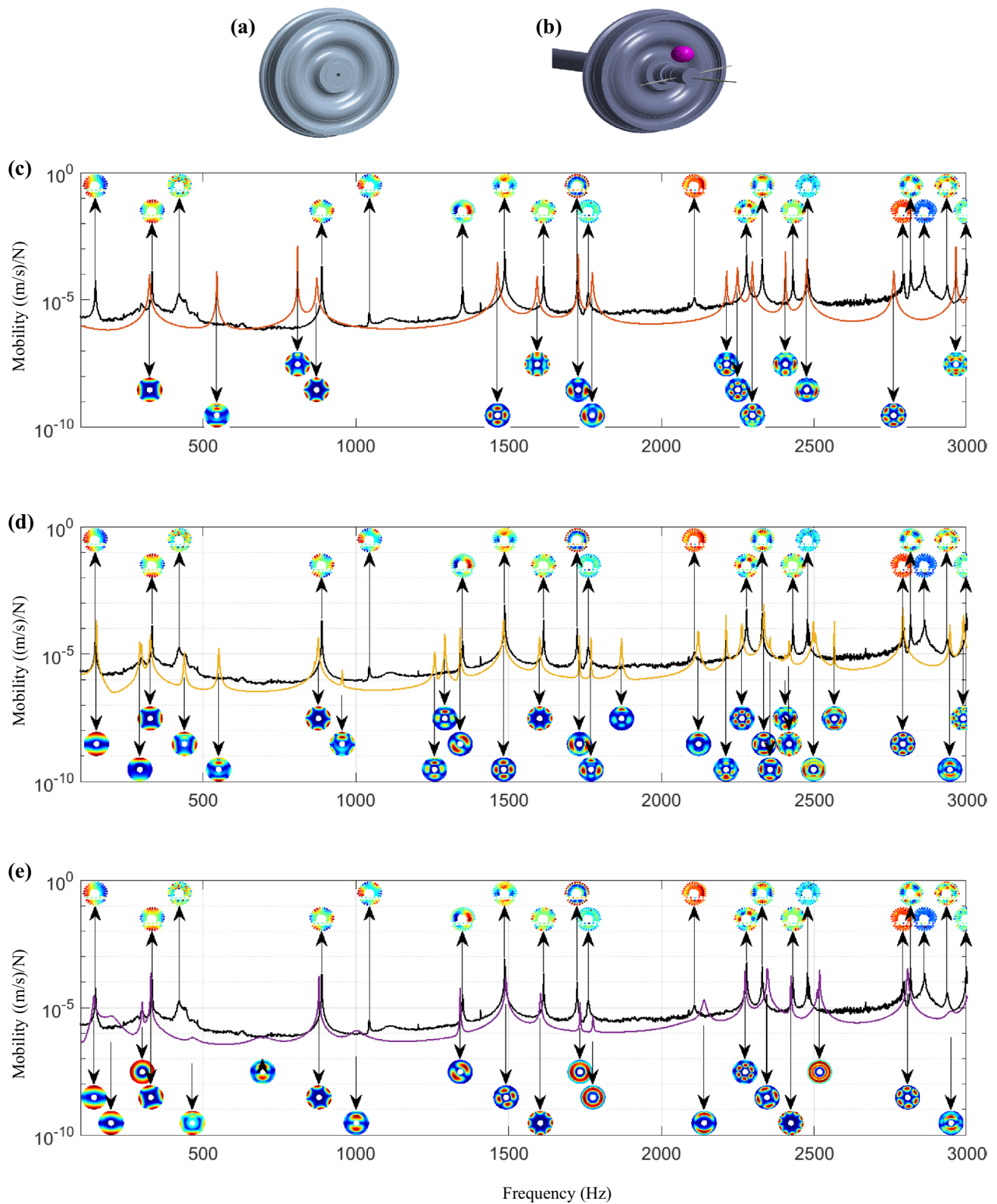


Fig. 13 Impact of axle's boundary conditions on wheel dynamics: **a** single wheel constrained at the axis of symmetry, **b** wheelset with mass, spring and damper elements at the axis, **c** the comparison of the experimental wheelset including roller bearings (black) compared to a single wheel in finite elements during point excitation in radial direction, **d** the comparison of the experiment compared to an entire wheelset, and **e** the entire wheelset constrained with dampers and a spring connected to a point mass

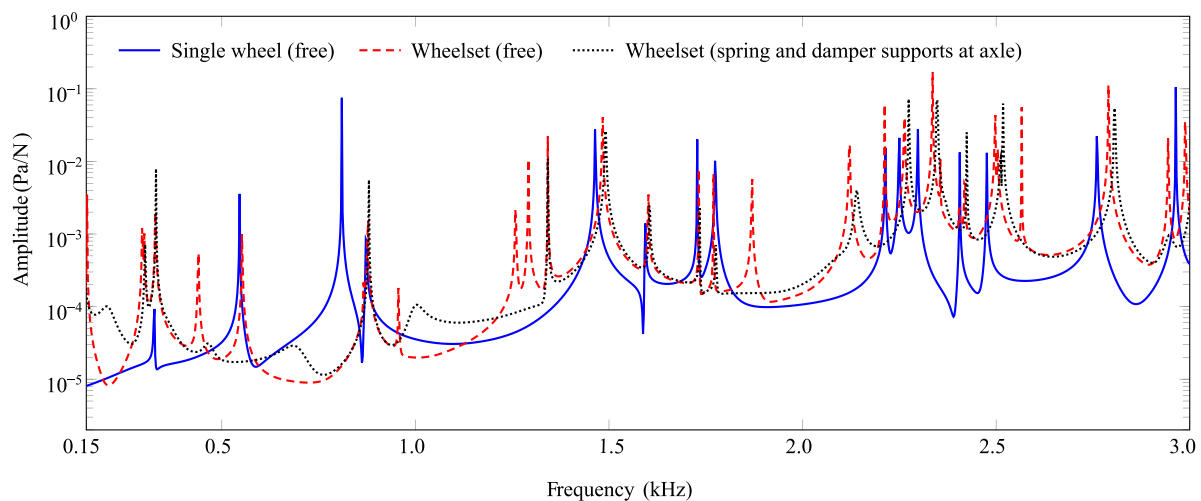


Fig. 14 Point pressure 7.5 m away and 1.2 m above the ground caused by a radial point force

model is essential for properly addressing the contact force, since it is heavily influenced by the dynamics of the wheel and rail and the roughness of both parts [1].

4.4 Computational complexity and discussion

By considering a railway wheelset, we investigate to what extent the discretized baffled piston considering DCM is applicable compared to other methods such as BEM and FEM. DCM and a discretized Rayleigh integral (DRI) are distinct concepts. The assumptions of DCM state that the vibrating surface can be discretized and split into the self- and mutual radiation impedance, as shown in Sect. 2.2.3. On the other hand, the baffled piston has geometrical limitations. First of all, complex surfaces such as curved wheels cannot be taken into account and need to be projected on a flat surface. In order to assess the curved geometry effect on acoustic radiation, in Appendix A, we compare emission from a curved wheel to the emission from a cylinder. For the case of the railway wheel, this projection is still precise enough for comparing it to the performed measurements. Secondly, sharp edges around the wheel and therefore edge radiation effects are not considered, since a baffled piston is by its definition a 2D object. This makes it especially difficult for objects close to reflective surfaces. If the wheel is located close to a hard boundary, only baffled modes can still be modeled precisely enough. For unbaffled modes, the DCM method deviates significantly from the BEM solution.

Comparing the three models, the baffled piston is the least computationally expensive. Only a single circular plane is discretized into elements, so fewer elements are needed. Also, no additional computational effort is required for surfaces and normal vectors, since all elements have the same size and orientation. On the other hand, the boundary

element model generally considers closed volumes and approximates more complex geometries with different types of meshes. This more than doubles the number of discretized surface elements and requires detailed calculations of surface properties such as the normal vector and area of each element, but still reduces computational effort a lot compared to the finite element method, which is computationally the most intensive method. Here, the entire volume must be discretized, and calculations in large distances become difficult as the number of elements increases considerably. For high frequencies, the mesh size must allow for at least six linear elements per wavelength. Considering the need to cover the standard audible range of railway wheels and rolling noise (50–6000 Hz), this makes FE calculation impractical. In this work, the valid range of the finite element model is from 200 up to 2000 Hz. By simply comparing the models in this frequency range, one gets a clear impression of the respective computational effort. For calculating the pressure for one frequency on the surface 0.88 m away from the source, the computational time for the baffled piston is approximately half the time taken for calculations of the BEM and less than 300 times the time taken for the FEM, see Table 1.

Table 1 Computational power for one frequency

Method	Nodes	Time (s)
Baffled piston with DCM	3,720	38.7
Boundary element method	880	72
Finite element method	9,122,444	13,200

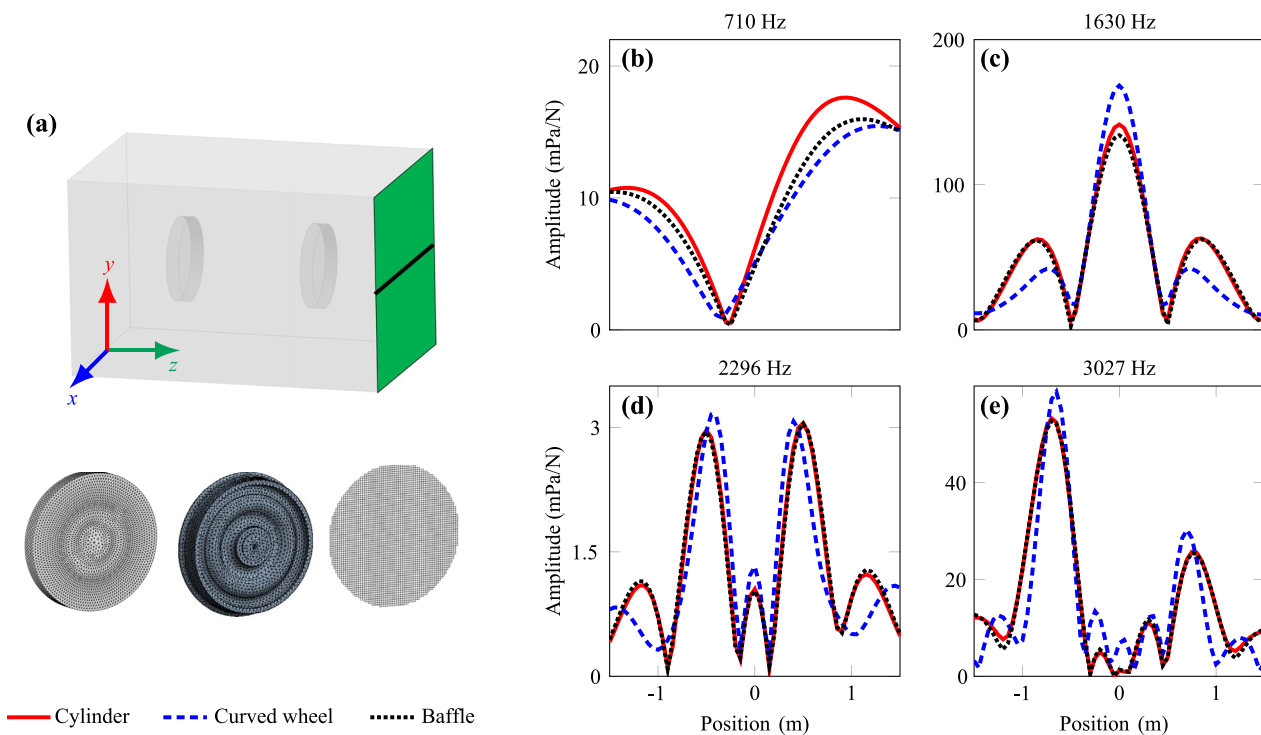


Fig. 15 Comparison of projected frontal velocities onto the cylinder (BEM) and the discretized baffle (DCM) to a curved wheel (BEM) taking into account all surface velocities (both front and back side): **a** schematic view of the numerical experiment, and **b–e** sound pressure per unit force for selected frequencies

5 Conclusions

We have studied the vibrational behavior and acoustic emission of a train wheelset. Detailed investigation of three mathematical models (baffled piston, boundary element method and finite element method) showed that the model of a vibrating disk mounted on an infinitely rigid baffle gives results comparable to BEM, as long as the system is subject to free-field conditions, meaning that the wheel emits into an open space without any reflective surfaces, and receiver points are located close to the central axis of the wheel. The thick web of the railway wheel acts like a baffle. As soon as reflections are taken into account, the edge radiation of the wheels has a significant impact on the final result for emitting wheel modes. This effect is amplified by the addition of a reflection plane, due to the proximity of the edge to the plane. The baffled piston model can therefore lead to significant modeling errors, since the edge radiation is not included there. Fluid–structure interaction in finite elements, on the other hand, is very time-consuming. Boundary conditions and mesh size require a large volume range to be valid for the entire frequency range from 50 to 2000 Hz. The limitation of the baffled piston is alleviated by the fact that a wheelset is in reality interacting with a rail, constraining the vibration at the edges. In future work, for precise results

including scattering effects, the BEM is the most accurate method and therefore recommended. However, due to the time efficiency, DCM can be useful to get fast and acceptable results for lab experiments.

Appendix A

Considering the potential interest in understanding the effects of projecting the surface velocities of a wheel just on the frontal faces of a discretized baffle (DCM) or a flat cylinder (BEM), we compare the two models with an authentic curved wheel geometry using BEM. The results are gathered through measurements along a line positioned at the same height as the axle center and at a 2-m distance away, see Fig. 15a. It becomes apparent that the mode shapes are effectively captured. However, the wheel's curved geometry considerably influences the magnitude and directionality, especially in proximity to the ranges furthest away from the center as seen in Fig. 15c, d and e. The magnitudes at peaks also demonstrate 10%–20% variations in cases of Fig. 15c, e. Despite these observations, the projection is capable of representing the modes and presents a suitable starting point when computational power is limited.

Acknowledgements The project was commissioned and supported by the funding of the Federal Office of Environment (No. 1337000438).

Open Access This article is licensed under a Creative Commons Attribution 4.0 International License, which permits use, sharing, adaptation, distribution and reproduction in any medium or format, as long as you give appropriate credit to the original author(s) and the source, provide a link to the Creative Commons licence, and indicate if changes were made. The images or other third party material in this article are included in the article's Creative Commons licence, unless indicated otherwise in a credit line to the material. If material is not included in the article's Creative Commons licence and your intended use is not permitted by statutory regulation or exceeds the permitted use, you will need to obtain permission directly from the copyright holder. To view a copy of this licence, visit <http://creativecommons.org/licenses/by/4.0/>.

References

- Thompson D (2009) Railway noise and vibration. Elsevier Ltd, Amsterdam
- Cui K, Qin X (2016) Numerical computation of wheel-rail impact noises with considering wheel flats based on the boundary element method. *J Vibroeng* 18(6):3930–3940
- Liu K, Jing L (2020) A finite element analysis-based study on the dynamic wheel-rail contact behaviour caused by wheel polygonization. *Proc Inst Mech Eng Part F: J Rail Rapid Transit* 234(10):1285–1298
- Thompson DJ, Fodiman P, Mahé H (1996) Experimental validation of the TWINS prediction program for rolling noise, part 2: results. *J Sound Vib* 193(1):137–147
- Thompson D, Squicciarini G, Zhang J et al (2018) Assessment of measurement-based methods for separating wheel and track contributions to railway rolling noise. *Appl Acoust* 140:48–62
- Hannema G, Tröbs H-M, Damme BV et al (2018) Validation of a FEM structure-borne sound radiation model for railway rolling noise. In: NOVEM 2018. Noise and vibration emerging methods (Ibiza, Spain)
- Jeong D, Choi HS, Choi YJ et al (2019) Measuring acoustic roughness of a longitudinal railhead profile using a multi-sensor integration technique. *Sensors* 19(7):1610
- Gutiérrez-Gil J, García-Andrés X, Martínez-Casas J et al (2019) Mitigation of railway wheel rolling noise by using advanced optimization techniques. In: EngOpt 2018 proceedings of the 6th international conference on engineering optimization, Lisboa, Portugal, 17–19 September 2019. Springer, pp 1141–1153
- Morin B, Plummer CJG, Kalyanasundaram B et al (2023) A fast analytical tool to investigate effects of railway superstructure components on track dynamics. In: The fifth international conference on railway technology: research, development and maintenance, (Montpellier). Elsevier, Amsterdam, pp 1–5
- Thompson D (1988) Predictions of acoustic radiation from vibrating wheels and rails. *J Sound Vib* 120(2):275–280
- Remington PJ (1976) Wheel/rail noise—Part I: characterization of the wheel/rail dynamic system. *J Sound Vib* 46(3):359–379
- Zhong T, Chen G, Sheng X et al (2018) Vibration and sound radiation of a rotating train wheel subject to a vertical harmonic wheel-rail force. *J Modern Transp* 26(2):81–95
- Thompson DJ, Jones CJC (2002) Sound radiation from a vibrating railway wheel. *J Sound Vib* 253(2):401–419
- Finnveden S, Fraggstedt M (2008) Waveguide finite elements for curved structures. *J Sound Vib* 312(4–5):644–671
- Fabre F, Theyssen JS, Pieringer A et al (2021) Sound radiation from railway wheels including ground reflections: a half-space formulation for the Fourier boundary element method. *J Sound Vib* 493:115822
- Squicciarini G, Thompson DJ, Toward MG et al (2015) The effect of temperature on railway rolling noise. *Proc Inst Mech Eng Part F: J Rail Rapid Transit* 230(8):1777–1789
- Fingberg U (1990) A model of wheel-rail squealing noise. *J Sound Vib* 143(3):365–377
- Thompson DJ, Jones CJ (2002) Sound radiation from a vibrating railway wheel. *J Sound Vib* 253(2):401–419
- Cutanda Henríquez V, Juhl PM (2010) OpenBEM—an open source boundary element method software in acoustics. In: Proceedings of INTER-NOISE 2010. 39th International Congress on Noise Control Engineering : noise and sustainability, Lisbon, Portugal, 13–16 June 2010. Curran Associates, Inc., pp 1–10
- Pritchard RL (1960) Mutual acoustic impedance between radiators in an infinite rigid plane. *J Acoust Soc Am* 32:730
- Arase EM (1964) Mutual radiation impedance of square and rectangular pistons in a rigid infinite baffle. *J Acoust Soc Am* 36:1521
- Stepanishen PR (1978) Evaluation of mutual radiation impedances between circular pistons by impulse response and asymptotic methods. *J Sound Vib* 59(2):221–235
- Schneider E, Popp K, Irretier H (1988) Noise generation in railway wheels due to rail-wheel contact forces. *J Sound Vib* 120(2):227–244
- Hashimoto N (2001) Measurement of sound radiation efficiency by the discrete calculation method. *Appl Acoust* 62(4):429–446
- Kolber K, Snakowska A, Kozupa M (2014) The effect of plate discretization on accuracy of the sound radiation efficiency measurements. *Arch Acoust* 39(4):511–518
- Bai M, Ih J-G, Benesty J (2013) Acoustic array systems: theory, implementation, and application. Wiley, New York
- Kirkup S (1998) The boundary element method in acoustics. Integrated Sound Software, Hebden Bridge
- Pierce AD (2019) Radiation from vibrating bodies. Springer, Cham, pp 177–239
- Santoni A, Bonfiglio P, Fausti P et al (2016) Sound radiation efficiency measurements on cross-laminated timber plates. In: Proceedings of the INTER-NOISE 2016. 45th international congress and exposition on noise control engineering. Towards a quieter future, (Hamburg), DEGA
- Strutt JW (2011) The theory of sound, vol 9781108032. Cambridge University Press, Cambridge
- Skudrzyk E (1971) The foundations of acoustics: basic mathematics and basic acoustics, 1st edn. Springer, Wien
- Porter DT (2005) Self- and mutual-radiation impedance and beam patterns for flexural disks in a rigid plane. *J Acoust Soc Am* 117(6):3415–3424
- Sha K, Yang J, Gan WS (2005) A simple calculation method for the self- and mutual-radiation impedance of flexible rectangular patches in a rigid infinite baffle. *J Sound Vib* 282(1–2):179–195
- Ansys Inc (2022) Theory reference ANSYS. 20th edn. Available from: <https://www.ansys.com/>
- Langer P, Maeder M, Guist C et al (2017) More than six elements per wavelength: the practical use of structural finite element models and their accuracy in comparison with experimental results. *J Comput Acoust* 25(04):1750025
- Brick H, Ochmann M (2008) A half-space BEM for the simulation of sound propagation above an impedance plane. *J Acoust Soc Am* 123(5):3418